Cell Reports
Physical Science

CellPress
OPEN ACCESS

Article

Recognition of RNA secondary structures with a programmable peptide nucleic acid-based platform

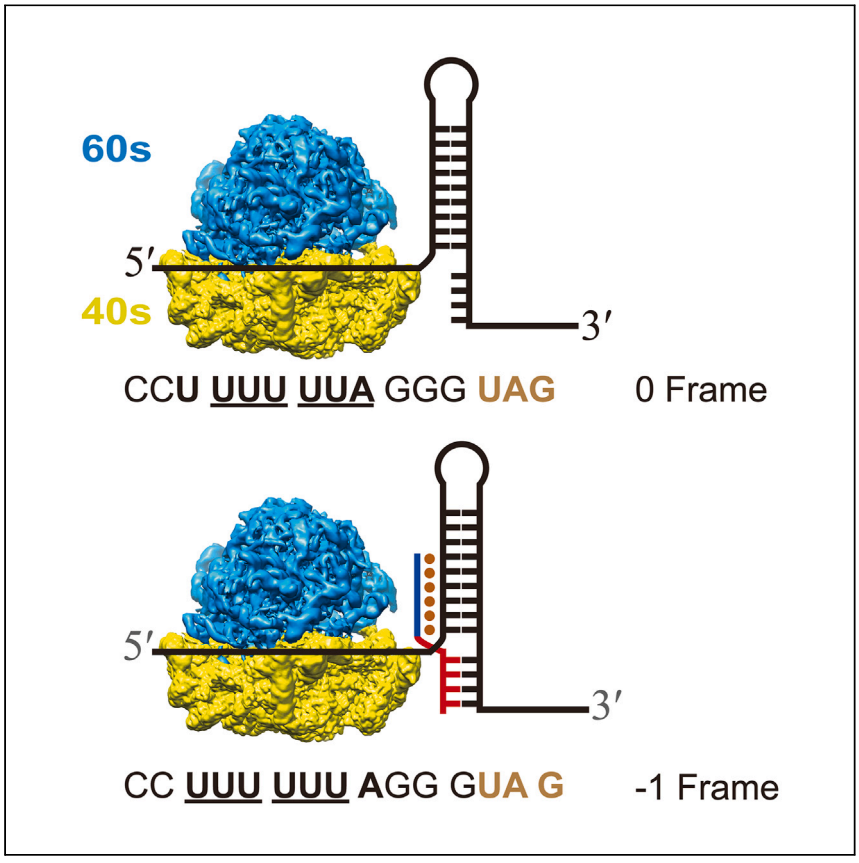

Lu et al. show that RNA structures can be targeted by a new type of peptide nucleic acids (daPNAs) through binding to dsRNA-ssRNA junctions. daPNAs bind to RNA structures with high sequence/structure specificity and strong binding affinity, with great potential in biomedical applications, including ribosomal frameshifting regulation.

Rongguang Lu, Liping Deng, Yun Lian, ..., Hongwei Wang, Guobao Li, Gang Chen

l3gb@qq.com (G.L.)
chengang@cuhk.edu.cn (G.C.)

Highlights

New RNA-binding mode with simultaneous recognition of dsRNA and ssRNA regions

RNA targeting by formation of a triplex next to a duplex at a dsRNA-ssRNA junction

Substrate-specific inhibition of Dicer acting on pre-miR-198

Targeting mRNA dsRNA-ssRNA junction for stimulating ribosomal frameshifting

Lu et al., Cell Reports Physical Science 5, 102150
September 18, 2024
Published by Elsevier Inc.
https://doi.org/10.1016/j.xcrp.2024.102150

Cell Reports
Physical Science

CellPress
OPEN ACCESS

Article

Recognition of RNA secondary structures with a programmable peptide nucleic acid-based platform

Rongguang Lu,[1,2,9] Liping Deng,[1,9] Yun Lian,[1,9] Xin Ke,[3,9] Lixia Yang,[4,9] Kun Xi,[1] Alan Ann Lerk Ong,[5] Yanyu Chen,[1] Hanting Zhou,[1] Zhenyu Meng,[5] Ruiyu Lin,[1] Shijian Fan,[1] Yining Liu,[1] Desiree-Faye Kaixin Toh,[5] Xuan Zhan,[1] Manchugondanahalli S. Krishna,[5] Kiran M. Patil,[5] Yunpeng Lu,[5] Zheng Liu,[1] Lizhe Zhu,[1] Hongwei Wang,[3] Guobao Li,[2,*] and Gang Chen[1,6,7,8,10,*]

SUMMARY

RNA secondary structures comprise double-stranded (ds) and single-stranded (ss) regions. Antisense peptide nucleic acids (asPNAs) enable the targeting of ssRNAs and weakly formed dsRNAs. Nucleobase-modified dsRNA-binding PNAs (dbPNAs) allow for dsRNA targeting. A programmable RNA-structure-specific targeting strategy is needed for the simultaneous recognition of dsRNAs and ssRNAs. Here, we report on combining dbPNAs and asPNAs (designated as daPNAs) for the targeting of dsRNA-ssRNA junctions. Our data suggest that combining traditional asPNA (with a 4-letter code: T, C, A, and G) and dbPNA (with a 4-letter code: T or s^2U, L, Q, and E) scaffolds facilitates RNA-structure-specific tight binding (nM to μM). We further apply our daPNAs in substrate-specific inhibition of Dicer acting on precursor miRNA (pre-miR)-198 in a cell-free assay and regulating ribosomal frameshifting induced by model hairpins in both cell-free and cell culture assays. daPNAs would be a useful platform for developing chemical probes and therapeutic ligands targeting RNA.

INTRODUCTION

RNAs perform diverse catalytic and regulatory functions in viruses and cells. RNA structures, critical for RNA functions, are mainly stabilized by base-paired double-stranded (ds) stem regions.[1,2] Together with single-stranded (ss) loop regions, RNAs can fold into complex secondary and tertiary structures,[3] facilitating the molecular recognition of RNA structures by small molecules[4–7] and peptides/proteins.[8,9] Antisense oligonucleotides (ASOs) are a successful class of RNA-targeting drugs, which bind to target RNAs by Watson-Crick base pairing. ASOs have already been approved for the treatment of certain diseases, such as Duchenne muscular dystrophy and spinal muscular atrophy.[10] ASOs typically range in size from 13 to 25 nucleotides (nt).[10]

Currently, programmable RNA structure-specific and tight-binding ligands are relatively unexplored. Triplex-forming oligonucleotides (TFOs) bind to the major groove of RNA duplexes through Hoogsteen and Hoogsteen-like base-pairing interactions (see Figure 1).[11] However, triplexes formed by traditional TFOs are often not stable due to the charge-charge repulsion among negatively charged phosphate backbones of three strands and strong pH dependence for the formation of C^+•G-C

[1]School of Medicine, The Chinese University of Hong Kong, Shenzhen (CUHK-Shenzhen), Shenzhen 518172, Guangdong, China

[2]National Clinical Research Center for Infectious Diseases, Shenzhen Clinical Research Center for Tuberculosis, Shenzhen Third People's Hospital, Shenzhen 518112, Guangdong, China

[3]School of Life Sciences, Tsinghua University, Beijing 100084, China

[4]School of Life Science and Technology, University of Electronic Science and Technology of China, Chengdu 610054, Sichuan, China

[5]Division of Chemistry and Biological Chemistry, School of Physical and Mathematical Sciences, Nanyang Technological University, Singapore 637371, Singapore

[6]Shenzhen Key Laboratory of Innovative Drug Synthesis, The Chinese University of Hong Kong, Shenzhen (CUHK-Shenzhen), Shenzhen 518172, Guangdong, China

[7]The Chinese University of Hong Kong, Shenzhen (CUHK-Shenzhen) Futian Biomedical Innovation R&D Center, Shenzhen 518031, Guangdong, China

[8]X (formerly Twitter): @ChenRNAChen

[9]These authors contributed equally

[10]Lead contact

*Correspondence: l3gb@qq.com (G.L.), chengang@cuhk.edu.cn (G.C.)

https://doi.org/10.1016/j.xcrp.2024.102150

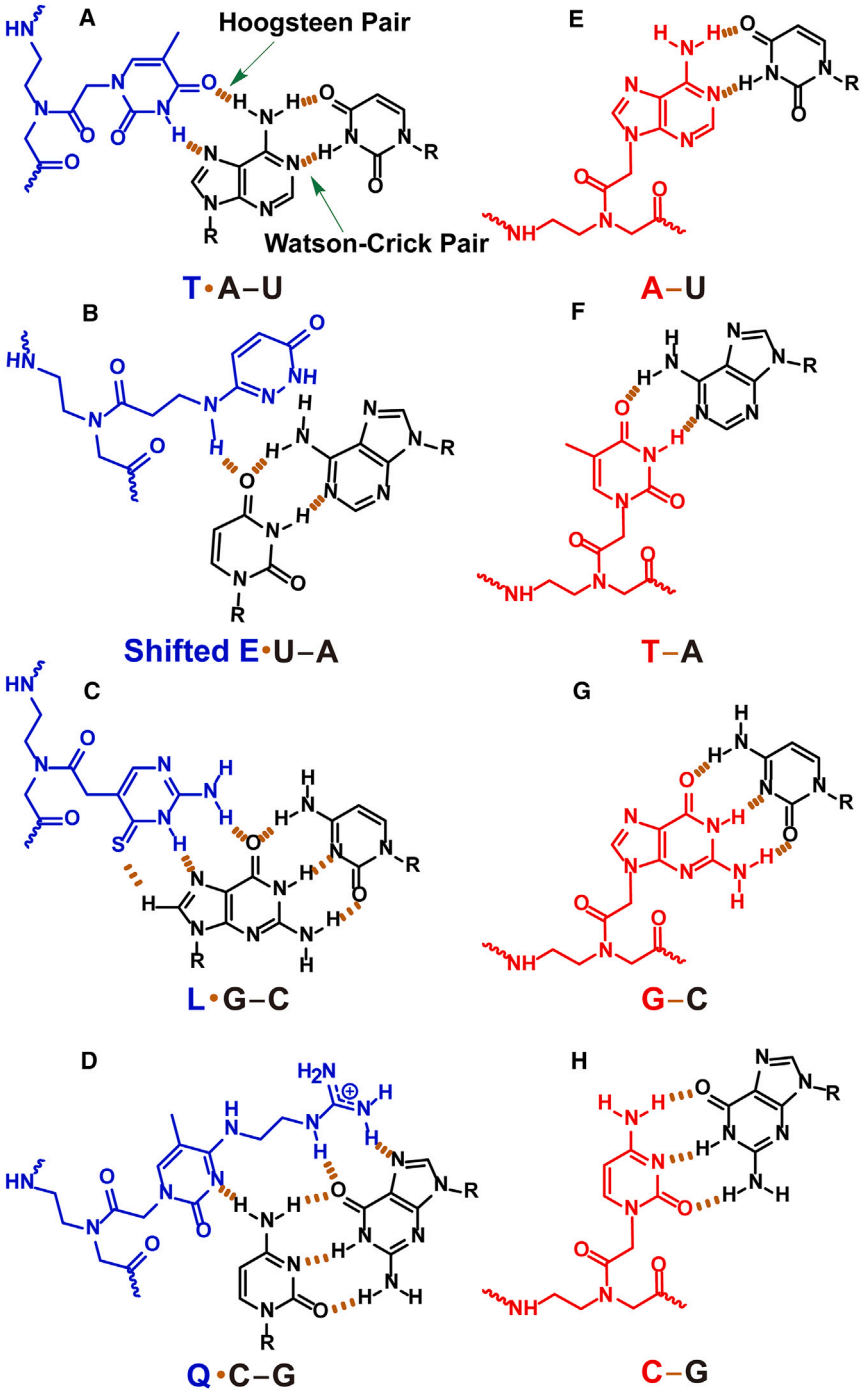

Figure 1. Chemical structures of base triples and base pairs formed between PNA and RNA

"R" represents the sugar-phosphate backbone of RNA. Hydrogen-bonding interactions are indicated by orange dashed lines.

(A–D) Base triples of T·A-U and shifted E·U-A, L·G-C, and Q·C-G[21] formed by dbPNA residues with RNA base pairs. Compared to the unmodified C base, the modified L base shows enhanced recognition of a G-C pair with reduced pH dependence.[22] The shifted E·U-A triple was drawn in a geometry[21] based on the previous study on backbone-base linker optimization.[23] The enhanced van der Waals interaction between the sulfur and hydrogen atoms is shown. The Hoogsteen and Watson-Crick pairs are shown as dots and lines, respectively. PNA and RNA are shown in blue and black, respectively. The base triple formation allows for the recognition of dsRNA regions.

Figure 1. *Continued*
(E–H) Base pairs of A-U, T-A, G-C, and C-G formed by asPNA with ssRNA. Unmodified PNA and RNA are shown in red and black, respectively. The base pairing between PNA and RNA allows the recognition of ssRNA regions.

base triple.[12–15] In addition, C-G and U-A base pairs are not easily recognized by natural nucleobases. Modifications on the sugar-phosphate backbone and nucleobases have been done to improve the properties of TFOs.[11,13,14,16,17] It is worth noting that TFOs containing unmodified and modified sugar-phosphate backbones often bind more strongly to dsDNAs than dsRNAs.[11,16–20]

Peptide nucleic acid (PNA) is characterized by a neutral, peptide-like backbone, which imparts chemical stability and nuclease resistance (Figure 1).[24] PNA-DNA and PNA-RNA duplexes are generally more stable than DNA-DNA and RNA-RNA duplexes.[25–27] Strong binding of a PNA to a complementary sequence allows the strand invasion of a dsRNA or a dsDNA, with one of the strands of the dsRNA/dsDNA displaced by the PNA. Importantly, PNAs show promising bioactivities in animal models.[28–35] However, traditional antisense PNAs (asPNAs) do not bind to RNAs by recognizing RNA structures, which may give rise to off-target binding.

We and others have shown that short (e.g., 10-mer) dsRNA-binding PNAs (dbPNAs) incorporated with modified nucleobases can form sequence-specific triplexes with dsRNAs through the formation of consecutive PNA•RNA-RNA base triples (Figures 1A–1D), with significantly weakened binding to dsDNAs and ssRNAs.[21,22,36–47] The dbPNAs have shown biological activities in stimulating ribosomal frameshifting,[48] inhibiting translation,[49] microRNA (miRNA) maturation,[39,50] RNA editing,[51] and viral RNA replication.[38] However, naturally occurring dsRNAs in functional RNAs are often interrupted by ssRNA loop regions, which may limit the application of dbPNAs. Thus, developing a scaffold for the simultaneous recognition of dsRNA and ssRNA regions is critical.

We herein designed novel PNAs combining dbPNAs (containing bases of T or s^2U, L, Q, and E or S; Figures 1A–1D and S1)[22,36,38,39,52] and traditional asPNAs (containing unmodified bases T, C, G, and A; Figures 1E–1H) (designated as daPNAs; see Figure 2) for the simultaneous recognition of dsRNA and immediately adjacent ssRNA regions. Binding data suggest that novel daPNAs can be utilized for targeting the dsRNA-ssRNA regions, including those found in model RNA hairpins, miRNA precursors, and tau pre-mRNA splice-site hairpins. Our cell-free and cell-based assays show that daPNAs exhibit biological activities. daPNAs can be utilized to target dsRNA-ssRNA regions with high sequence/structure specificity and strong binding affinity, potentially overcoming the obstacles encountered by other techniques, such as small molecules and traditional ASOs, including asPNAs.

RESULTS AND DISCUSSION

daPNA binds to model dsRNA-ssRNA junction and stimulates ribosomal frameshifting

We designed a series of short daPNAs with the asPNA segment antiparallel to the ssRNA region and the dbPNA segment forming a parallel triplex with the dsRNA region (see Figures 2A and 2E for a schematic view and see all the PNAs studied in Table S1; Figures S2–S6). Our structural modeling study following the reported method[37,53] suggests that such a novel fold with a major-groove dbPNA·dsRNA triplex next to an asPNA-ssRNA duplex at a dsRNA-ssRNA junction is structurally compatible without significant distortion in the backbones and bases

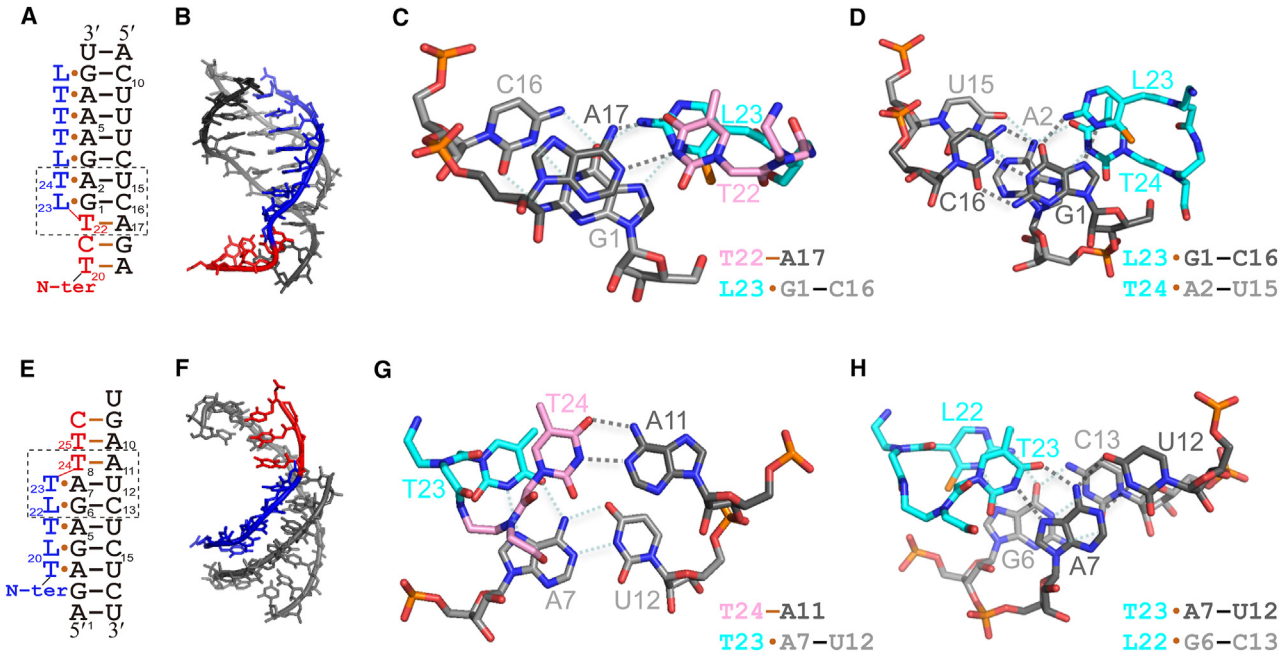

Figure 2. Modeled structures of daPNA-RNA complexes

(A–D) A modeled daPNA•(dsRNA-ssRNA) structure with the N-terminal segment of the PNA forming a PNA-RNA duplex.

(A and B) Secondary structure scheme and modeled structure with the RNA and PNA residues shown in black and color, respectively.

(C and D) Detailed stacking patterns in the triplex-duplex junctions with the carbon atoms for the bases of RNAs and PNAs shown in black and color, respectively.

(E–H) A modeled daPNA•(dsRNA-ssRNA) structure with the C-terminal segment of the PNA forming a PNA-RNA duplex.

(E and F) Secondary structure scheme and modeled structure with the RNA and PNA residues shown in black and color, respectively.

(G and H) Detailed stacking patterns in the triplex-duplex junctions with the carbon atoms for the bases of RNAs and PNAs shown in black and color, respectively.

(Figures 2B, 2F, S7, and S8). The detailed structures of the dsRNA-ssRNA junctions in complex with daPNAs are shown in Figures 2C, 2D, 2G, and 2H. It is interesting to observe that, at the junction, there is much more base stacking in the case with the asPNA residue upstream of the dbPNA residue (Figure 2C), compared to the case with the asPNA residue downstream of the dbPNA residue (Figure 2G). Importantly, the junction structures complexed with daPNAs are largely stable with a force field[54] in the modeling even without base-base hydrogen-bonding restraints, although local dynamics are observed, with the RNA-RNA Watson-Crick pairs at the ssRNA-dsRNA junction partially disrupted (Figure S8).

We constructed a hairpin rHP1-5t containing a 5 nt 3′ dangling end (overhang) as a model of dsRNA-ssRNA junction (Figure 3A). We made a 10-mer daPNA da5t (NH_2-Lys-AGAGTLTLTT-$CONH_2$) targeting rHP1-5t (Figures 3A and 3B). The 10-mer daPNA da5t contains an N-terminal 4-mer segment (AGAG) for the formation of an antiparallel PNA-RNA duplex with the 3′ dangling end and a C-terminal 6-mer dbPNA segment (TLTLTT) for the formation of a major-groove PNA•dsRNA triplex (Figures 2 and 3A). We carried out nondenaturing polyacrylamide gel electrophoresis (PAGE) and biolayer interferometry (BLI) assays to characterize the recognition of the model dsRNA-ssRNA junction by PNAs (Figures 3C and 3D). Nondenaturing PAGE data suggest that da5t indeed binds tightly to rHP1-5t (K_D = 4 nM) (Figures 3C, 3E, S9, and S10). However, da5t shows no binding with rHP1-3t, with a 5′ dangling end with the same ssRNA sequence as rHP1-5t (Figures 3A, 3E, S9, and S10). Consistent with the PAGE results, BLI data demonstrated that da5t can bind to rHP1-5t with

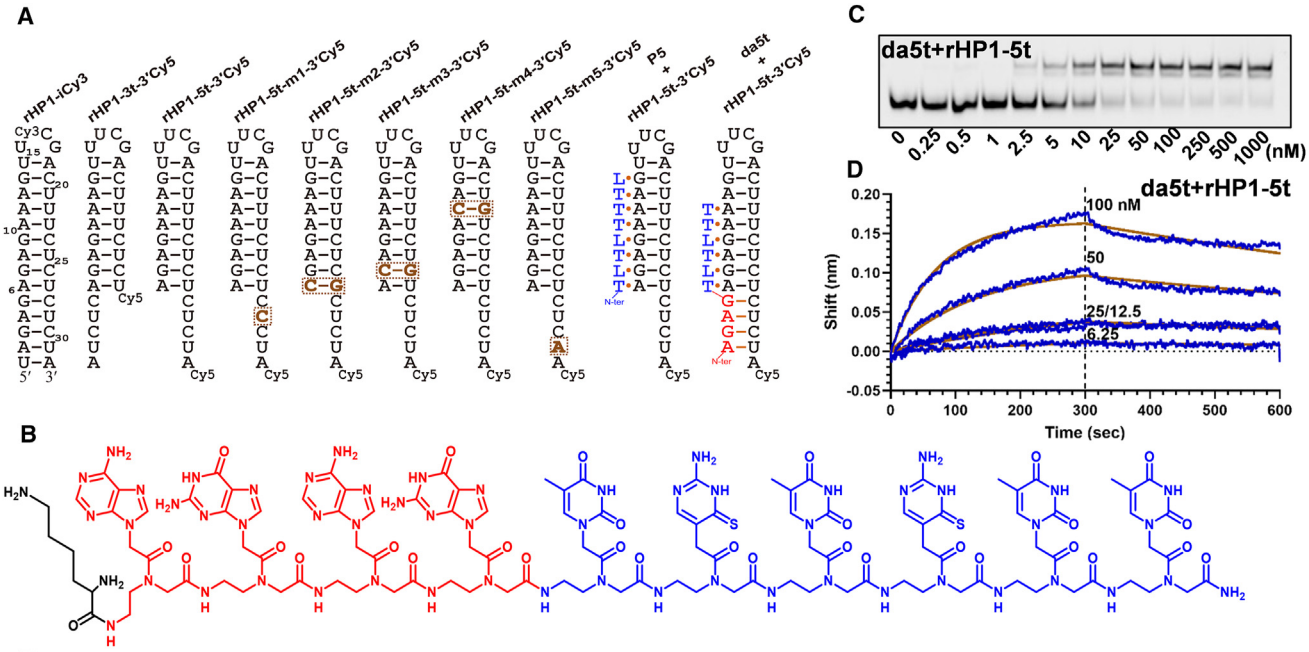

E The binding parameters determined by bio-layer interferometry and PAGE.

PNA	RNA	PAGE	bio-layer interferometry			
		K_D (nM)	K_D (nM)	k_{on} (M^{-1} s^{-1})	k_{off} ($\times 10^{-6}$ s^{-1})	R^2
P5	rHP1	288±29 (180±70)	3790±276	456±2	1730±5	0.99
da5t	rHP1	No binding	No binding	—	—	—
P5	rHP1-5t	110±25	—	—	—	—
da5t	rHP1-5t	4±1	7±1	132,000±412	884±4	0.99
P5	rHP1-5t-m1	67±17	—	—	—	—
da5t	rHP1-5t-m1	15±3	13±1	63,600±686	841±10	0.96
da5t	rHP1-5t-m2	Weak binding	Weak binding	—	—	—
da5t	rHP1-5t-m3	No binding	No binding	—	—	—
da5t	rHP1-5t-m4	4±1	—	—	—	—
da5t	rHP1-5t-m5	7±1	—	—	—	—
P5	rHP1-3t	108±27	—	—	—	—
da5t	rHP1-3t	No binding	No binding	—	—	—

Figure 3. Targeting model RNAs with dsRNA-ssRNA junctions

(A) RNA constructs and schematics of a dbPNA and a daPNA binding to rHP1-5t.

(B) Chemical structure of daPNA da5t (NH_2-Lys-AGAGTLTLTT-$CONH_2$). The dbPNA and asPNA segments are shown in blue and red, respectively. The lysine residue (black) is in L configuration.

(C and D) Representative binding data of PNA da5t with rHP1-5t base on nondenaturing PAGE and BLI assays, respectively. For the PAGE assay, the concentrations of PNA are 0, 0.25, 0.5, 1, 2.5, 5, 10, 25, 50, 100, 250, 500, and 1,000 nM and for the BLI assay are 6.25, 12.5, 25, 50, and 100 nM.

(E) Binding parameters obtained by nondenaturing PAGE and BLI. The errors shown are standard errors. The data shown in the parentheses are from Ong et al.[39]

a K_D of 7 nM but with no significant binding to rHP1-3t (Figures 3D, 3E, and S9–S11). The data suggest that the asPNA segment of a daPNA forms an antiparallel duplex, but not a parallel duplex, with ssRNA in a dsRNA-ssRNA junction. Furthermore, da5t does not bind with rHP1, which has no ssRNA dangling end, as determined by PAGE and BLI assays (Figures 3E and S9–S11). Taken together, our data suggest that daPNA binds to the dsRNA-ssRNA junction structure with structure specificity.

We subsequently generated five rHP1-5t mutants (rHP1-5t-m1, rHP1-5t-m2, rHP1-5t-m3, rHP1-5t-m4, and rHP1-5t-m5) with U29C, A6C&U27G, G7C&C26G, A11C&U22G, and U31A mutations, respectively (Figure 3A), to test the sequence specificity of da5t. Both the PAGE and BLI results revealed that da5t has a weakened binding to rHP1-5t-m1 (Figures 3E and S9–S11), indicating that the asPNA segment of da5t is an important part of a daPNA in binding with an RNA structure. rHP1-5t-m2 and rHP1-5t-m3 have the single base pair mutation at the junction and adjacent to the dsRNA-ssRNA junction, respectively (Figure 3A). da5t shows significantly weakened or no binding to rHP1-5t-m2 and rHP1-5t-m3 (Figures 3E and S9–S11), suggesting that an internal base triple is critical for da5t binding. rHP1-5t-m4 and rHP1-5t-m5 have the single base pair mutation and single base mutation at the terminal ends, respectively (Figure 3A). The PAGE results show that rHP1-5t-m4 and rHP1-5t-m5 show comparable K_D values (4 ± 1 and 7 ± 1 nM) to rHP1-5t (Figures 3E, S9, and S10), indicating that the terminal base triple or base pair may be flexible and the disrupted hydrogen-bonding interactions may be compensated by stacking interactions with adjacent residues. A daPNA negative control (da5t-NC; NH_2-Lys-TGTATAQLL-$CONH_2$) shows no observable binding with rHP1-5t (Figures S9 and S10). We previously reported that a dbPNA (P5) forms a triplex with rHP1 (Figure 3A) with a K_D of about 200 nM.[22,48] Compared to da5t, dbPNA P5 binds to rHP1, rHP1-5t, and rHP1-3t with a similar but comparably weakened binding affinity (Figures 3E, S9, and S10).[48]

We next performed ultraviolet (UV) absorbance-detected thermal melting assay to characterize the thermal stabilities of complexes formed between da5t and different RNA constructs (Figures 3A and S12). The melting data reveal that rHP1 and rHP1-5t have melting temperature values of 85°C and 76°C, respectively (Figures S12A and S12B). Remarkably, da5t-rHP1-5t has a one-step melting transition with a melting temperature of around 85°C (Figure S12B), consistent with the formation of a tightly bound complex. Interestingly, there may be a broad melting transition (around 40°C–70°C) for the sample with da5t and rHP1 mixed (Figure S12A). We speculate that the bottom stem of rHP1 may have increased breathing dynamics at temperatures above around 50°C, which facilitates the binding of da5t, although da5t shows no binding at lower temperatures, as evidenced by BLI (assay temperature 30°C) and PAGE (assay temperature 4°C) experiments. rHP1-5t-m1 and rHP1-5t-m2 in complex with da5t also show broad transitions (around 40°C–70°C) (Figures S12C and S12D). rHP1-5t-m3 and rHP1-5t-m4 in complex with da5t seem to show relatively lower melting temperatures of about 45°C and 58°C, respectively (Figures S12E and S12F). The comparative thermal melting data suggest that the novel complex formed between a daPNA and a dsRNA-ssRNA junction has a high thermal stability and may be sensitive to the presence of mismatched base pairs/triples at relatively high temperatures.

We further applied daPNAs in targeting mRNA structures for translational regulation. Programmed −1 ribosomal frameshifting (PRF) is a recoding mechanism utilized by many RNA viruses to express viral proteins in the −1 frame and 0 frame with defined ratios. The mRNA elements important for PRF include a slippery sequence (e.g., U UUU UUA in 0 frame and UUU UUU A in −1 frame), an ss spacer (about 8 nt), and a downstream mRNA structure (Figures 4A–4C).[55–60] The dual-luciferase reporter assay (Figure 4A) is a documented method for studying PRF.[48,61,62] We previously reported that dbPNA P5 (Figures 3A and 4D) forms a triplex with rHP1 and stimulates PRF efficiency by enhancing the stability of rHP1 at the ribosomal entry site.[22,48]

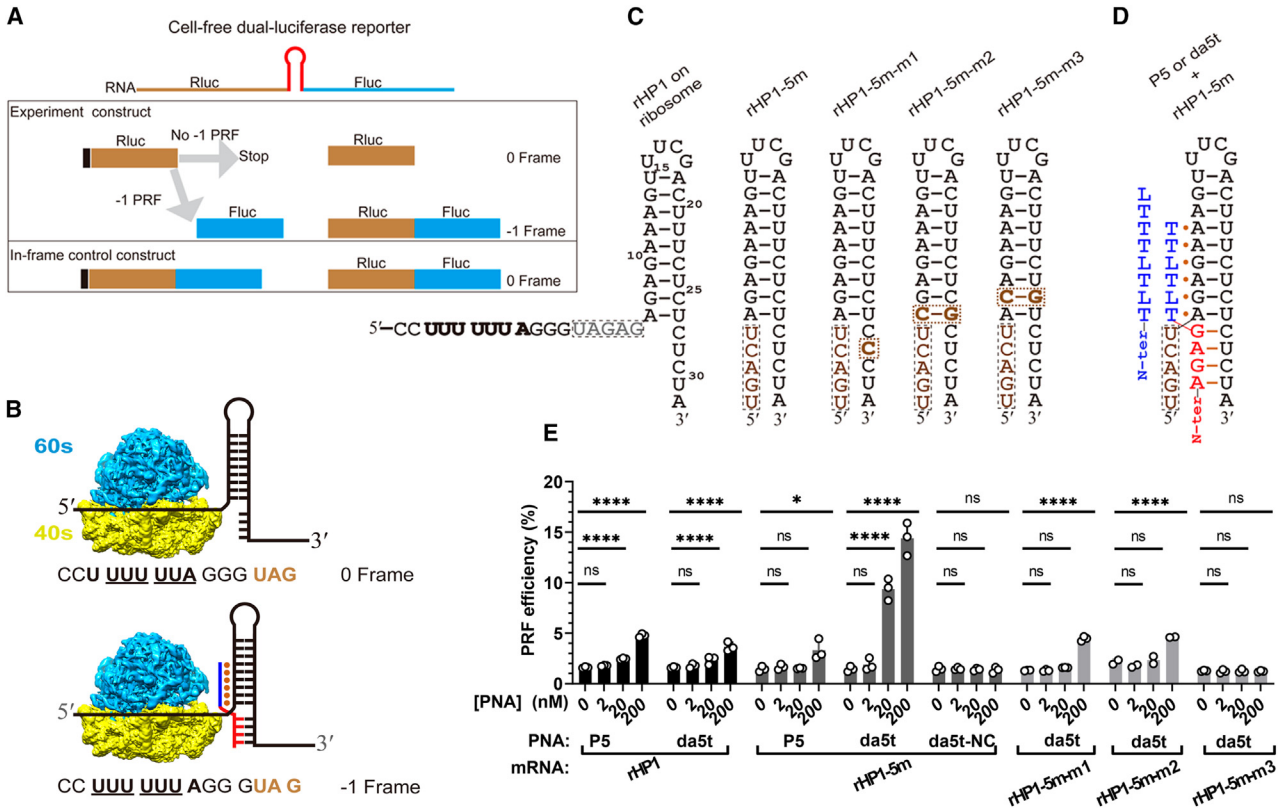

Figure 4. Schematic of dual-luciferase reporter system for measuring PRF efficiency and cell-free dual-luciferase reporter assay data for dbPNA and daPNA targeting model RNA hairpins

(A) Schematic of the dual-luciferase reporter to determine the programmed −1 ribosomal frameshifting (PRF) efficiency in the cell-free system.

(B) Ribosome positioned at slippery site with partially open rHP1 RNA structure at the mRNA entry site. A −1 ribosomal frameshifting results in the reading frame shifted from 0 frame (U UUU UUA) to −1 frame (UUU UUU A), causing the readthrough of the stop codon UAG (shown in brown) at the 0 frame. daPNA binding at the dsRNA-ssRNA junction at the mRNA entry site results in an enhanced −1 ribosomal frameshifting.

(C) Secondary structures of rHP1 with the bottom 5 base pairs unwound by ribosome positioned at the slippery site and rHP1-5m and mutants. The mutated residues are shown in brown.

(D) Schematic of dbPNA P5 and daPNA da5t binding to rHP1-5m. (E) Cell-free dual-luciferase reporter assay data for dbPNA and daPNA targeting model RNA hairpins. The data were analyzed by GraphPad Prism 9.3 and calculated by an ordinary one-way analysis of variance (ANOVA) using Dunnett's multiple comparisons test against the mean of mRNA alone group. The error bars represent ± S.D. *$p < 0.05$, **$p < 0.01$, ***$p < 0.001$, ****$p < 0.0001$, and ns, not significant.

Herein, we employed the dual-luciferase reporter assay to test if daPNA binding to mRNA structures affects PRF. We hypothesize that daPNA binding to mRNA structure at the ribosome entry site with a ribosome positioned at the slippery site (Figures 4B–4D) may temporarily inhibit the elongating ribosome's helicase activity in unwinding mRNA secondary structure.[63,64] With a ribosome positioned at the slippery site, it is expected that the bottom five base pairs of rHP1 are unwound, resulting in the formation of a ribosome-induced dsRNA-ssRNA junction identical to that of rHP1-5t (Figures 3A, 4B, and 4C). We also made mRNA constructs rHP1-5m and rHP1-5m-m1/rHP1-5m-m2/rHP1-5m-m3 to mimic the ribosome-independent dsRNA-ssRNA junction structures present in rHP1-5t and rHP1-5t-m1/rHP1-5t-m2/rHP1-5t-m3, respectively (Figures 3A and 4C). The schematic of the dual-luciferase reporter plasmid (pDL) is shown in Figure 4A, with the inserted sequences verified by sequencing (Table S3; Figure S13A). Cell-free dual-luciferase reporter assay data show that rHP1, rHP1-5m, rHP1-5m-m1, rHP1-5m-m2, and rHP1-5m-m3 have similar PRF efficiencies of 1.9% ± 0.1%, 1.5% ± 0.2%, 1.3% ± 0.1%, 1.9% ± 0.1%, and 1.3% ± 0.1%, respectively. Consistent with our previous report,[48]

applying 200 nM dbPNA P5 results in moderately enhanced PRF efficiencies of 4.8% ± 0.2% and 3.3% ± 1.0%, for rHP1 and rHP1-5m, respectively (Figures 4E, S14A, and S14B).

Consistent with the proposed binding of daPNA da5t to the mRNA dsRNA-ssRNA junction at the ribosome entry site (Figures 4B–4D), applying 200 nM da5t causes significantly enhanced PRF efficiency of rHP1-5m (14.8% ± 1.6%) (Figure 4E). da5t binds to rHP1-5m in the absence of an elongating ribosome, as the dsRNA-ssRNA junction structure is independent of a ribosome positioned at the slippery site (Figure 4D). Interestingly, da5t also moderately stimulates the PRF efficiency of mRNA rHP1 (Figure 4E), even though da5t shows no binding to short free hairpin rHP1 (Figure 3E). Note that both cell-free translation and BLI assays were done at 30°C. It is likely that the ribosome positioned at the slippery site results in the unwinding of the bottom 5 base pairs of the rHP1 structure in the mRNA (Figures 4B and 4C), with the intermediate structure allowing for the binding of da5t resulting in frameshifting stimulation. It is important to note that applying da5t stimulates the expression of the Firefly luciferase (Fluc) but not the Renilla luciferase (Rluc) (Figures S14A and S14B). Applying a control PNA da5t-NC at 200 nM shows no observable change in the PRF efficiency of rHP1-5m (Figures 4E, S14A, and S14B).

rHP1-5m-m1 and rHP1-5m-m2/rHP1-5m-m3 have a single base mutation and a single base pair mutation, respectively, in the ssRNA and dsRNA regions of rHP1-5m (Figure 4C). As expected, rHP1-5m-m1 and rHP1-5m-m2 show a much-reduced response to the application of da5t in stimulating frameshifting, with rHP1-5m-m3 showing no response to the addition of da5t (Figures 4E, S14A, and S14B). Taken together, our cell-free dual-luciferase data clearly suggest that da5t binds to the dsRNA-ssRNA junction, resulting in a highly sequence- and structure-specific enhancement of ribosomal frameshifting.

We further employed a dual-fluorescent reporter (enhanced green fluorescent protein [EGFP]/monomer cherry protein [mCherry]) assay to determine the effect of daPNA on PRF efficiency in cell culture.[8,56] We constructed a dual-fluorescent reporter plasmid (pDF) derived from pcDNA5 vector, which contains a P2A ribosome skip signal sequence downstream of the frameshifting stimulation elements between EGFP and mCherry coding sequences (Figure 5A; Table S3). 24 h after the plasmid and PNA transfection into human embryonic kidney 293T (HEK293T) cells, each cell that showed an EGFP fluorescence signal was used for the PRF efficiency analysis (Figure S15). The mCherry level shows no correlation with the EGFP level, indicating that the plasmid transfection efficiency does not significantly affect the PRF efficiency (Figure S15). The cell-based assay using the pDF reporter system gives a PRF efficiency value of 4.5% ± 0.2% for rHP1-5m (Figure 5B). da5t shows potent cellular activity in stimulating PRF efficiency in a dose-dependent manner, with an efficiency of 9.2% ± 0.9% at 10 μM (Figure 5B). However, applying 10 μM P5 only results in a slight increase of PRF efficiency to 5.6% ± 0.4% (Figure 5B). da5t shows no clearly observable activity in stimulating the PRF of rHP1-5m-m1 (Figure 5B), indicating that the cellular activity is sequence specific. Importantly, da5t only stimulates the expression of mCherry, with the EGFP expression unchanged (Figures S14C and S14D). A histogram analysis of the PRF efficiency of individual EGFP-active cells clearly suggests that da5t is a specific stimulator of PRF of rHP1-5m (Figures 5C and S15). We tested if the cellular mRNA levels change by applying daPNA da5t. Our qPCR data show that da5t shows no observable effect on the mRNA expression levels of EGFP and ATP binding cassette subfamily E member 1, a ribosome recycling factor, which may affect ribosomal frameshifting (Figure S16).[65] Thus, our data show that da5t exerts a

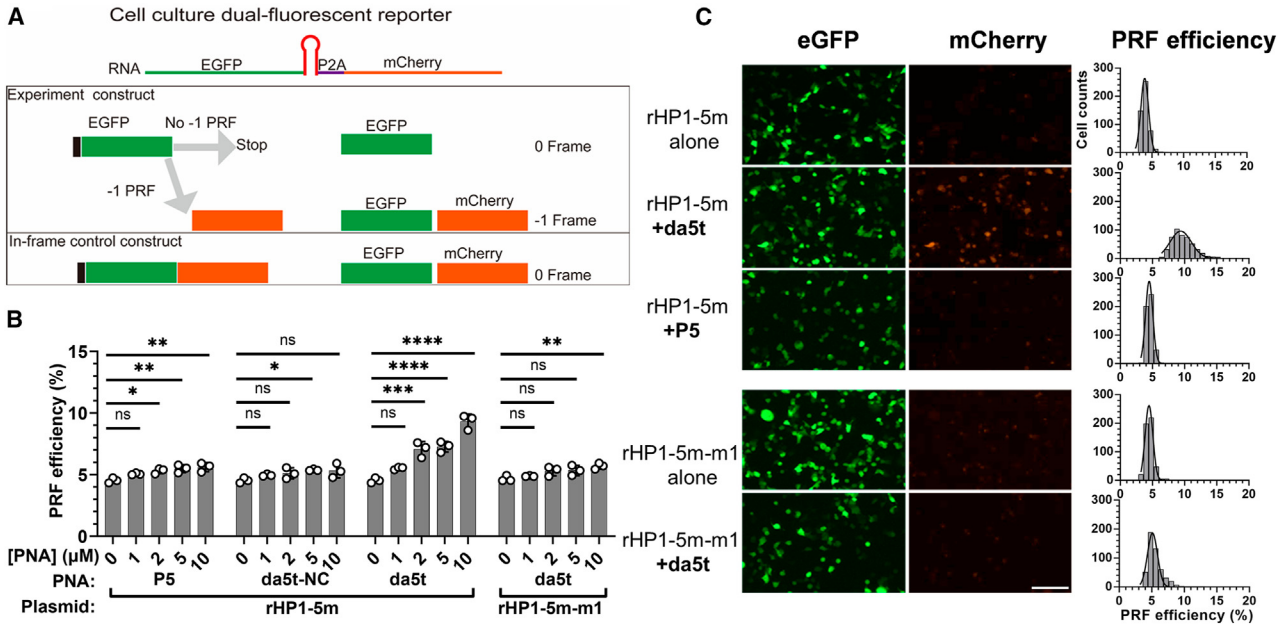

Figure 5. Schematic of dual-fluorescent reporter (EGFP/mCherry) system for measuring PRF efficiency and cell culture dual-fluorescent reporter assay data for dbPNA and daPNA targeting model RNA hairpins

(A) Schematic of the dual-fluorescent reporter.

(B) PRF efficiency stimulated by daPNA in cell culture. See the PNA sequences in Figure 4.

(C) Representative fluorescence imaging data and histogram analysis (summary from three independent assays) of PRF efficiencies of EGFP-positive cells with and without 10 μM PNAs. Scale bar, 50 μm. The data were analyzed by GraphPad Prism 9.3 and calculated by an ordinary ANOVA using Dunnett's multiple comparisons test against the mean of plasmid alone group. The error bars represent ± S.D. *$p < 0.05$, **$p < 0.01$, ***$p < 0.001$, ****$p < 0.0001$, and ns, not significant.

frameshifting stimulation effect through directly binding to the mRNA structure. Furthermore, the confocal microscopic imaging assay data show that fluorescein (FAM)-labeled dat5t (da5t-FAM) is taken up by HEK293T cells aided by the transfection reagent Lipofectamine 3000 (Figure S17). Clearly, cellular activity of daPNA may be further improved by enhancing the daPNA cell uptake efficiency. da5t shows no apparent toxicity in HEK293T cells up to a concentration of 10 μM (Figure S18). Together, our data suggest that daPNA molecules are useful in targeting mRNA structures at the ribosomal entry site for stimulating ribosomal frameshifting.

daPNAs targeting pre-miRNA-198 inhibit Dicer cleavage activity

We next tested the generality of the application of the daPNA platform by designing a daPNA targeting a biomedically important regulatory precursor miRNA (pre-miR), pre-miR-198 (Figure 6A).[39,66] We previously demonstrated that an 8-mer dbPNA, db-198 (NH_2-Lys-LLTL2TLL-$CONH_2$, 2: s^2U; see Figure S1), binds to pre-miR-198 with a K_D = 80 nM (Figure S19).[39] In this study, we made a daPNA by adding three adenine residues at the C-terminal side of db198 (da198-AAA, NH_2-Lys-LLTL2TLLAAA-$CONH_2$) (Figure 6A). We characterized the binding properties by nondenaturing PAGE and BLI (Figures 6B and 6C). As expected, the nondenaturing PAGE data show that, compared to the original dbPNA (db198), da198-AAA shows enhanced binding (K_D = 10 nM) (Figures 6B–6D, S19, and S20). The BLI results also show that da198-AAA (K_D = 278 nM) has a stronger binding than db198 (K_D = 784 nM) with pre-miR-198 (Figures 6C, 6D, and S21).

We subsequently generated three pre-miR-198 mutants (pre-miR-198-m1, pre-miR-198-m2, and pre-miR-198-m3) with residues at 30–33 changed from UUUU to AACC

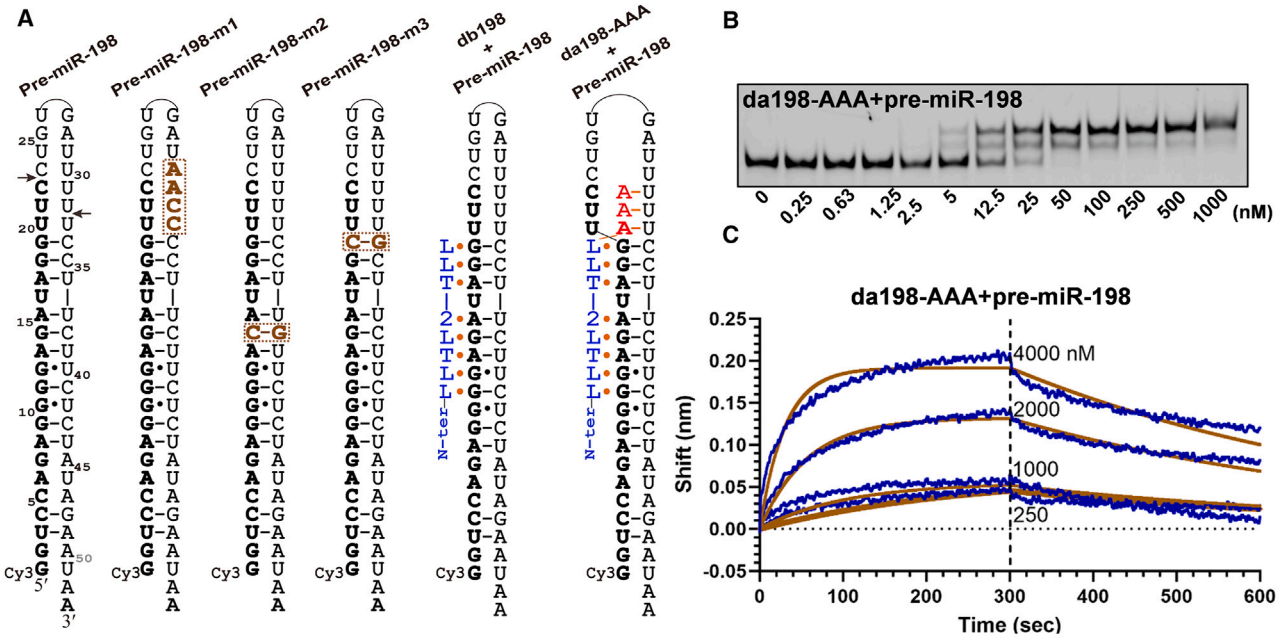

D

The binding parameters determined by bio-layer interferometry and PAGE.

PNA	RNA	PAGE	bio-layer interferometry			
		K_D (nM)	K_D (nM)	k_{on} (M^{-1} s^{-1})	k_{off} (10^{-6} s^{-1})	R^2
db198	Pre-miR-198	80±19	784±5	2260±9	1770±5	0.99
da198-AAA	Pre-miR-198	10±3	278±3	7740±52	2150±10	0.96
db198	Pre-miR-198-m1	248±46	—	—	—	—
da198-AAA	Pre-miR-198-m1	163±23	—	—	—	—
db198	Pre-miR-198-m2	No binding	—	—	—	—
da198-AAA	Pre-miR-198-m2	No binding	—	—	—	—
db198	Pre-miR-198-m3	1023±170	—	—	—	—
da198-AAA	Pre-miR-198-m3	80±22	—	—	—	—
da198-AAA	Pre-miR-21	No binding	—	—	—	—

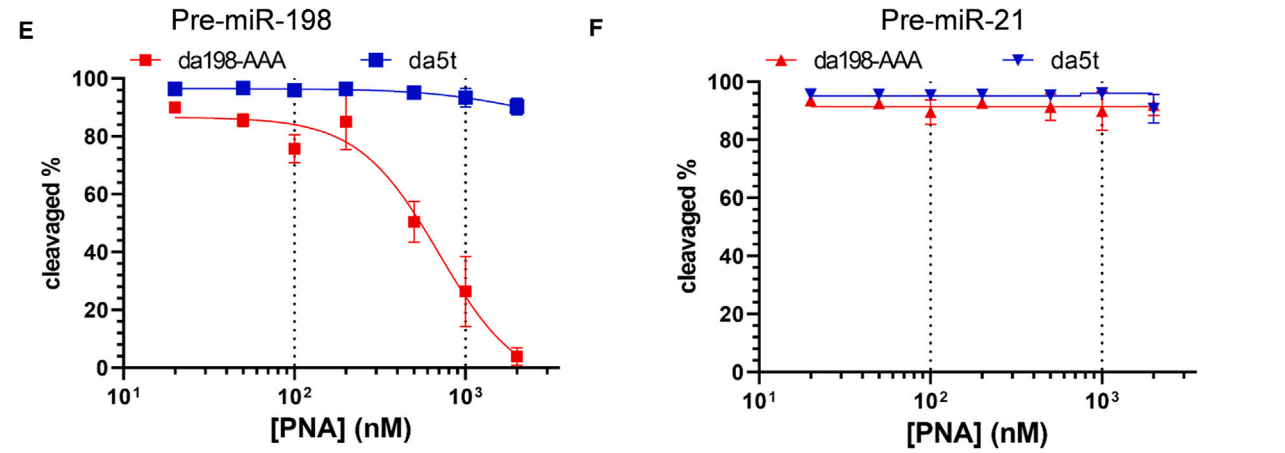

Figure 6. daPNAs binding to pre-miR-198 and inhibition of Dicer enzyme cleavage activity

(A) Schematic of pre-miR-198 hairpin targeting by dbPNA db198 and daPNA da198-AAA. The mature miR-198 sequence is shown in bold. The Dicer cleavage sites for pre-miR-198 are indicated by arrows. The mutated RNA constructs are shown with the mutated residues shown in brown.

Figure 6. *Continued*

(B and C) Representative binding data of PNA da198-AAA with pre-miR-198 base on nondenaturing PAGE and BLI assays, respectively. For the PAGE assay, the concentrations of PNA are 0, 0.25, 0.63, 1.25, 2.5, 5, 12.5, 25, 50, 100, 250, 500, and 1,000 nM and for the BLI assay are 4,000, 2,000, 1,000, and 250 nM.

(D) Binding parameters obtained by nondenaturing PAGE and BLI. The errors shown are standard errors.

(E and F) Cell-free Dicing data show that daPNA da198-AAA designed for targeting pre-miR-198 inhibits the Dicer cleavage activity specifically on pre-miR-198. The errors shown are standard deviations.

and G14C&C38G and G19C&C34G mutations, respectively (Figure 6A), to test the sequence specificity of da198-AAA. The nondenaturing PAGE data show that pre-miR-198-m1 binds to da198-AAA with a K_D of 163 $\pm$ 23 nM, which is about 16-fold weaker than that of pre-miR-198 (Figures 6D, S19, and S20). However, the K_D of 248 $\pm$ 46 nM for pre-miR-198-m1 with db198 is only 3-fold weaker than that of pre-miR-198 (Figures 6D, S19, and S20). These results demonstrate that the PNA-RNA duplex formation between the asPNA part of da198-AAA and the loop region U residues of pre-miR-198 significantly enhances the binding affinity. Furthermore, pre-miR-198-m2 shows no binding to either da198-AAA or db198 (Figures 6D, S19, and S20) suggesting that an internal PNA·RNA-RNA base triple formation is critical for RNA structure recognition. Compared with pre-miR-198, pre-miR-198-m3 shows significantly weakened binding to da198-AAA (K_D = 80 $\pm$ 22 nM) and db198 (K_D = 1,023 $\pm$ 170 nM) (Figures 6D, S19, and S20). The data suggest that a PNA·RNA-RNA base triple formed at the dsRNA-ssRNA junction region is also important for RNA structure recognition.

We further tested if the newly made db198-AAA can inhibit pre-miR-198 maturation catalyzed by Dicer. The Dicer cleavage assay data show that da198-AAA can specifically inhibit the Dicer cleavage activity on pre-miR-198, but not pre-miR-21, *in vitro* (Figures 6E, 6F, S22, and S23). Taken together, our data show that daPNA platform molecules are useful in sequence and structure specifically targeting RNA structures for inhibiting Dicer and other enzymes acting on RNA.

Applications of daPNAs in binding to tau pre-mRNA splice-site hairpin

Finally, we tested the application of the daPNA platform for targeting tau pre-mRNA splice-site hairpin structure (Figure S24A). The tau pre-mRNA hairpin structure (Figure S24A) is located at the exon 10-intron 10 junction.[67–71] Point mutations in this splice-site hairpin structure result in (de)stabilizing of the hairpin and thus aberrant alternative splicing, leading to neurodegenerative diseases such as frontotemporal dementia with 15 Parkinsonism linked to chromosome 17.[69–74] Significantly, our nondenaturing PAGE result suggests that a 9-mer daPNA da-tau (NH_2-Lys-TQTQTGCCG-$CONH_2$) (Figure S24B) binds strongly to the tau pre-mRNA splice-site hairpin (tau-Cy3) at 200 mM NaCl (pH 7.5; K_D = 27 $\pm$ 11 nM; Figure S24B). The advantage of a daPNA compared to a traditional asPNA is that daPNA is sequence and structure specific and has a relatively lower energy barrier for melting the preformed RNA structures. In this case, the relatively weak bottom stem of the tau pre-mRNA splice hairpin structure[70,74] is targeted by strand invasion by a 5-mer asPNA segment of da-tau to form a PNA-RNA duplex, which is presumably cooperatively stabilized by a 4-base-triple PNA•dsRNA triplex.

In summary, we have developed a novel and generally applicable binding mode by combining dbPNA and asPNA for the recognition of a dsRNA region and an immediately adjacent ssRNA region (dsRNA-ssRNA junction) through the simultaneous formation of an asPNA-RNA duplex and a major-groove dbPNA·RNA_2 triplex. A dsRNA-ssRNA junction structure can be preformed or induced by the binding of daPNAs (through the strand invasion of weakly formed dsRNA regions) or generated

by helicases such as a translating ribosome. We demonstrated the application of the new molecular recognition strategy by targeting a series of RNA structures. Dicer cleavage activity data suggest that daPNAs can be used to inhibit miRNA maturation in a substrate-specific manner. Cell culture data show that daPNAs are effective in stimulating ribosomal frameshifting. Thus, the daPNA platform would serve as programmable junction-specific molecular glues for the probing and targeting of many biologically and medically essential RNA structures in transcriptomes, including mRNA, long noncoding RNA, and many other noncoding RNAs.

EXPERIMENTAL PROCEDURES

Resource availability

Lead contact

Further requests for information should be directed to and will be fulfilled by the lead contact, Gang Chen (chengang@cuhk.edu.cn).

Materials availability

This study did not generate new unique materials.

Data and code availability

This study did not generate/analyze datasets/code.

Synthesis of PNA and RNA oligomers

Reverse-phase high-performance liquid chromatography (RP-HPLC)-purified terminally Cy3-labeled, Cy5-labeled, and internally Cy3-labeled RNAs were purchased from Sigma-Aldrich and BioSynTech China, respectively. The PNA monomers thymine (T), cytosine (C), guanine (G), and adenine (A) were purchased from ASM Research Chemicals. PNA monomers L, Q, E, and S were synthesized following the reported methods.[22,23,36,75] PNA oligomers were synthesized manually using Boc chemistry via a solid-phase peptide synthesis protocol. 4-Methylbenzhydrylamine hydrochloride polystyrene resins were used. The loading value used for synthesizing the oligomers was 0.3 mmol/g, and acetic anhydride was used as the capping reagent. Benzotriazol-1-yl-oxytripyrrolidinophosphonium hexafluorophosphate and *N,N*-diisopropylethylamine were used as the coupling reagent. The oligomerization of PNA was monitored by the Kaiser test. Cleavage of the PNA oligomers was done using the trifluoroacetic acid (TFA) and trifluoromethanesulfonic acid method, after which the oligomers were precipitated with diethyl ether, dissolved in deionized water, and purified by RP-HPLC using water-CH_3CN-0.1% TFA as the mobile phase. LC-tandem mass spectrometry was used to characterize the oligomers. The extinction coefficients of A, G, T, s^2U, C, L, and Q were estimated to be 15.4, 11.7, 8.8, 10.2, 7.3, 7.3, and 7.3 mM^{-1} cm^{-1}, respectively, at 260 nm.

Molecular modeling

We modeled the structure based on the major-groove PNA•RNA-RNA triplex structure from our previously studied models.[37] A three-base-pair PNA-RNA duplex segment was firstly extracted from a reported structure (PDB: 1PNN), and then we connected the PNA-RNA duplex segment to the remaining PNA•RNA-RNA triplex structure. Subsequently, the obtained structure was solvated by TIP3P water molecules, followed by optimization and constant temperature, constant volume (NVT) and constant temperature, constant pressure (NPT) equilibrium. Then, a 100 ns product Molecular Dynamics (MD) simulation was conducted with the trajectory used for clustering. The centered structure of the most populated cluster was regarded as the representative structure. The structures were then all subject to

energy minimization and NVT/NPT equilibrium, followed by a 30 ns simulated annealing (SA; with temperature steps of 298→448→448→298 K). Specifically, the system temperature was heated from 298 K to 448 K in 10 ns, followed by a 10 ns production run at 448 K, and finally cooled back to 298 K in 10 ns. For the complexes with both the PNA•RNA-RNA triplex and PNA-RNA duplex simultaneously formed, an additional 60 ns SA simulation was done (298→498→498→298→498→498→298 K). During the SA, all base-base hydrogen bonds were restrained (distance restraint: 0.0-0.3 nm (with a cut-off distance of 0.4 nm) and 1,000 kJ/mol/nm^2; angle restraint: 180° and 5.0 kJ/mol/rad^2).

UV absorbance detected thermal melting assay

Thermal melting curves were obtained using a Shimadzu 2550 spectrometer. The buffer for the melting experiment contains 200 mM NaCl, 0.5 mM EDTA, and 20 mM HEPES (pH 7.5). The samples were prepared by heating at 95°C for 5 min, followed by slow cooling. The concentrations of RNA and PNA were both 5 μM. The absorbance at 260 nm was recorded with increasing temperature from 20°C to 95°C with a ramp rate of 0.5°C/min.

Nondenaturing PAGE

The nondenaturing PAGE (20%, bis:arc = 29:1) experiments were performed using an incubation buffer containing 200 mM NaCl, 0.5 mM EDTA, and 20 mM HEPES (pH 7.5). For the labeled RNAs, the concentration was kept at 5,10, or 20 nM with varied PNA concentrations in 20 μL of buffer. Snap cooling was done for RNA hairpins by directly dipping the sample tubes from 95°C into an ice bath and annealing with PNAs by slow cooling from 65°C to room temperature. The sample tubes were incubated for 2–4 h at 4°C before the loading. To all the samples, 35% glycerol (20% of the total loaded volume) was added, followed by vortexing for a few seconds before loading into the sample wells of the gels. Using a running buffer 1× TBE (Tris-borate-EDTA; pH 8.3), the gels were run at 4°C for 5 h with a voltage set at 250 V for all the experiments. The gels were imaged using an Amersham Imager 680.

BLI assay

The BLI assay was performed using a Gator Prime (GatorBio). The 3′ biotin-RNA samples (BioSynTech) were diluted by binding buffer (containing 200 mM NaCl, 0.5 mM EDTA, and 20 mM HEPES [pH 7.5]) into 200 nM final concentration. The concentrations of PNAs are varied for da5t (100, 50, 25, 12.5, and 6.25 nM) and db198 and da198-AAA (4,000, 2,000, 1,000, 500, and 250 nM). The association and dissociation time periods are both 300 s at 30°C.

Plasmid construction

The PRF efficiency in a cell-free system was determined by p2luc plasmid (pDL for brevity).[61] As described previously, the model RNA (rHP1) served as an experiment construct, and an in-frame control plasmid was constructed by disrupting the slippery sequences, with 100% PRF efficiency. To generate plasmids pDL-rHP1-5m, rHP1-5m-m1, rHP1-5m-m2, and rHP1-5m-m3, the according sequences (Table S3) were inserted into the p2luc vector using the BmHI and SacI restriction enzyme site. Furthermore, a dual-fluorescence (pDF for brevity) reporter based on the pcDNA5 vector was employed to determine the PRF efficiency in cell culture assay. The sequences of rHP1-5m and rHP1-5m-m1 (Table S3) were inserted between the EGFP and mCherry coding sequences into the pcDNA5 vector BamHI and XhoI restriction enzyme site. The plasmids were extracted using Monarch Plasmid Miniprep kit (NEB) and precipitated by cold ethanol. The quality and concentration of plasmid DNA were measured by the NanoDrop One spectrophotometer (Thermo Scientific). Plasmids with various

mutations were generated by PCR methods using Q5 Site-Directed Mutagenesis Kit (NEB) according to the instructions and verified by Sangon (China).

DNA linearization and transcription

PCR was employed to prepare linearized DNA based on primers pDL-631 and pDL-3431 using Q5 Hot Start PCR polymerase (NEB). All the components were mixed well and incubated in a thermal cycler (Bio-Rad) under the following procedure: 95°C for 30 s; 35 cycles of 95°C for 30 s, 57°C for 30 s, 72°C for 2 min; and 72°C for 2 min. The PCR products were precipitated by cold ethanol. The transcription process was driven by T7 polymerase using HiScribe T7 High Yield RNA Synthesis Kit (NEB). After 2 h transcription, the DNA template was removed by DNase I (NEB) digestion, and the RNA transcripts were purified by the RNA Transcript Purification Kit (NEB) and dissolved in RNase-free double-distilled H_2O.

In vitro translation

Translation protocols were described previously with minor modifications.[48] In brief, 0.02 μM mRNA (final concentration) was mixed with various concentrations of PNAs and the appropriate volume of the rabbit reticulocyte lysate system (Promega). The translation mixtures were incubated at 30°C for 90 min followed by the dual-luciferase reporter assay (Promega). The 2 μL translation products were added into a white 384-well microplate (PerkinElmer), and then 20 μL Dual-Glo reagent (Promega) and the relative luminescence units were measured using an Envision microplate reader (PerkinElmer) under the ultra-sensitive model. After the Fluc luminescence was measured, 20 μL Dual-Glo Stop reagent (Promega) was added into the above mixture to measure the Rluc luminescence. The PRF efficiency was calculated under the formula[61]

$$\text{PRF efficiency}(\%) = \frac{(\text{FlucE}) \div (\text{RlucE})}{(\text{FlucC}) \div (\text{RlucC})} \times 100\%.$$

Here, FlucE and FlucC are the Fluc luminescence intensities of experimental and control samples, respectively. RlucE and RlucC are the Rluc luminescence intensities of experimental and control samples, respectively. Each experiment was performed at least thrice, and data were analyzed by GraphPad Prism 9.3 using the one-way ANOVA method.

Dual fluorescent reporter assay

HEK293T (CRL-3216) was a gift provided by Prof. Lei Yong. About 5×10^3 cells/well were seeded into 384-well cell culture plates and cultured in Dulbecco's modified Eagle's medium (Gibco) supplemented with 10% fetal bovine serum (BI), 100 U/mL penicillin, and 100 μg/mL streptomycin (Sangon) at 37°C in 5% CO_2. The next day, 100 ng dual-fluorescent reporter plasmids with various concentrations of PNAs were co-transfected into cells using lipo3000 (Invitrogen) according to the instructions. After transfection for 24 h, the EGFP and mCherry signals were imaged by the Lionheart FX Automated Microscope (BioTek) with a 4× objective under laser focus mode. The total intensities of EGFP and mCherry were transformed into gray-scale and analyzed by CellProfiler Analyst with a threshold value of 0.15. The in-frame control plasmid with the slippery site disrupted was used as a control for calculating the PRF efficiency with the formula

$$\text{PRF efficiency}(\%) = \frac{(\text{mCherryE}) \div (\text{EGFPE})}{(\text{mCherryC}) \div (\text{EGFPC})} \times 100\%.$$

Here, mCherryE and mCherryC are the mCherry fluorescence intensities of experimental and control samples, respectively. EGFPE and EGFPC are the EGFP fluorescence intensities of experimental and control samples, respectively. Each

experiment was performed at least three times, and data were analyzed by GraphPad Prism 9.3 using the one-way ANOVA method.

PNA cell uptake assay

da5t-FAM with a final concentration of 10 μM was transfected into HEK293T cells using Lipofectamine 3000. 24 h after transfection, the wells were carefully wash by PBS three times. The distribution of da5t-FAM in cells was observed by confocal microscopy LSM 900 (Zeiss). FAM fluorescence was visualized with an excitation wavelength of 488 nm and an emission wavelength of 518 nm.

qPCR assay

The HEK293T cells were seeded into a 12-well plate, and after 24 h, da5t with a final concentration of 10 μM was transfected into cells using Lipofectamine 3000. After 24 h, the total RNAs were extracted using FreeZol Reagent (Vazemy) and reverse transcribed into cDNA using HiScript III All-in-one RT SuperMix Perfect for qPCR (Vazemy). The qPCR experiment was performed on a real-time PCR instrument QuantStudio 3 (Applied Biosystems) using the comparative Ct ($2^{-\Delta\Delta Ct}$) method and based on the Taq Pro Universal SYBR qPCR Master Mix (Vazemy).

Cell viability assay

The HEK293T cells were seeded into a 96-well plate and transfected PNA using Lipofectamine 3000 with final concentrations of 40, 20, 10, 5, 2.5, 1.25, 0.63, 0.31, and 0 μM. After 24 h, the Cell Counting Kit-8 was employed to determine the cell viability following the instruction (Sangon). The absorption signals at 450 nm were collected using a microplate reader (Bioteck).

In vitro dicing assay

The protocol for the *in vitro* dicing assay was described previously.[76] Cy3-labeled pre-miR-198 and pre-miR-21 RNA oligomers synthesized by BioSynTech was used in the dicing assay. The final concentrations of hDicer and pre-miR are 100 and 10 nM, respectively. PNAs with varied concentrations were pre-incubated with RNA at 50°C for 10 min and then slow cooled to room temperature. After hDicer was added, the dicing system was incubated at 37°C for 90 min. The reaction was stopped with 2× RNA loading buffer containing 8 M urea, 1×TBE, and 0.05% Bromophenol blue; boiled for 10 min; and subsequently chilled on ice. RNA products were analyzed on 15% polyacrylamide, 8 M urea denaturing gel electrophoresis and visualized with a Typhoon Trio Imager (Amersham Biosciences).

SUPPLEMENTAL INFORMATION

Supplemental information can be found online at https://doi.org/10.1016/j.xcrp.2024.102150.

ACKNOWLEDGMENTS

We thank Prof. Sam Butcher for sharing the experimental protocols and providing the p2luc plasmids, which were originally constructed by Prof. John Atkins and Raymond Gesteland. We thank Prof. Yongjuan Zhao and Dr. Yunjun Ge for their helpful suggestions on performing the dual-luciferase reporter assay. We thank Prof. Liang Yang for his help using the Lionheart FX Automated Microscope (BioTek).

This work was funded by a National Natural Science Foundation of China (NSFC) project (grant 22177098 to G.C.); The Chinese University of Hong Kong, Shenzhen (CUHK-Shenzhen) University Development Fund (to G.C.); a fund from the Shenzhen-Hong Kong Cooperation Zone for Technology and Innovation (HZQB-KCZYB-2020056 to

G.C.); the Shenzhen Science and Technology Innovation Committee for the Shenzhen Key Laboratory Scheme (ZDSYS20220507161600001); the Shenzhen Third People's Hospital Research Fund (24250G1021); a China Postdoctoral Science Foundation-funded project (2023M742416); the Shenzhen Clinical Research Center for Tuberculosis (20210617141509001); Guangdong Provincial Basic and Applied Basic Research Fund Project-Youth funding (2022A1515110577 to X.Z.); and the Ganghong Young Scholar Development Fund (PhD studentship) (to L.D.).

AUTHOR CONTRIBUTIONS

G.C., R. Lu, G.L., H.W., and Z.L. conceived this project. L.D., R. Lin, Y. Liu, Z.X., A.A.L.O., M.S.K., K.M.P., and D.-F.K.T. synthesized the PNA oligomers. L.D., Y. Lian, Y.C., and A.A.L.O. performed the PAGE experiments. R. Lu, Y. Lian, Y.C., and H.Z. performed the BLI assay. R. Lu, S.F., Y.C., H.Z., and L.Y. performed the cell-free dual-luciferase and cell culture dual-fluorescent reporter assays. X.K. performed the Dicer enzyme cleavage activity assay. K.X., Z.M., Y. Lu, Z.L., and L.Z. performed the molecular simulation study.

DECLARATION OF INTERESTS

A patent application based on some of the work reported here has been filed.

Received: February 1, 2024
Revised: June 13, 2024
Accepted: July 19, 2024
Published: August 12, 2024

REFERENCES

1. Turner, D.H. (2013). Fundamental interactions in RNA: Questions answered and remaining. Biopolymers *99*, 1097–1104. https://doi.org/10.1002/bip.22294.

2. Vicens, Q., and Kieft, J.S. (2022). Thoughts on how to think (and talk) about RNA structure. Proc. Natl. Acad. Sci. USA *119*, e2112677119.

3. Dethoff, E.A., Boerneke, M.A., Gokhale, N.S., Muhire, B.M., Martin, D.P., Sacco, M.T., McFadden, M.J., Weinstein, J.B., Messer, W.B., Horner, S.M., and Weeks, K.M. (2018). Pervasive tertiary structure in the dengue virus RNA genome. Proc. Natl. Acad. Sci. USA *115*, 11513–11518.

4. Tong, Y., Lee, Y., Liu, X., Childs-Disney, J.L., Suresh, B.M., Benhamou, R.I., Yang, C., Li, W., Costales, M.G., Haniff, H.S., et al. (2023). Programming inactive RNA-binding small molecules into bioactive degraders. Nature *618*, 169–179.

5. Thomas, J.R., and Hergenrother, P.J. (2008). Targeting RNA with small molecules. Chem. Rev. *108*, 1171–1224.

6. Childs-Disney, J.L., and Disney, M.D. (2016). Approaches to Validate and Manipulate RNA Targets with Small Molecules in Cells. Annu. Rev. Pharmacol. Toxicol. *56*, 123–140.

7. Warner, K.D., Hajdin, C.E., and Weeks, K.M. (2018). Principles for targeting RNA with drug-like small molecules. Nat. Rev. Drug Discov. *17*, 547–558.

8. Zimmer, M.M., Kibe, A., Rand, U., Pekarek, L., Ye, L., Buck, S., Smyth, R.P., Cicin-Sain, L., and Caliskan, N. (2021). The short isoform of the host antiviral protein ZAP acts as an inhibitor of SARS-CoV-2 programmed ribosomal frameshifting. Nat. Commun. *12*, 7193.

9. Chen, Y., Yang, F., Zubovic, L., Pavelitz, T., Yang, W., Godin, K., Walker, M., Zheng, S., Macchi, P., and Varani, G. (2016). Targeted inhibition of oncogenic miR-21 maturation with designed RNA-binding proteins. Nat. Chem. Biol. *12*, 717–723.

10. Shen, X., and Corey, D.R. (2018). Chemistry, mechanism and clinical status of antisense oligonucleotides and duplex RNAs. Nucleic Acids Res. *46*, 1584–1600.

11. Devi, G., Zhou, Y., Zhong, Z., Toh, D.F.K., and Chen, G. (2015). RNA Triplexes: from structural principles to biological and biotech applications. Wiley Interdiscip. Rev. RNA *6*, 111–128.

12. Sugimoto, N., Wu, P., Hara, H., and Kawamoto, Y. (2001). pH and cation effects on the properties of parallel pyrimidine motif DNA triplexes. Biochemistry *40*, 9396–9405.

13. Rusling, D.A., Powers, V.E.C., Ranasinghe, R.T., Wang, Y., Osborne, S.D., Brown, T., and Fox, K.R. (2005). Four base recognition by triplex-forming oligonucleotides at physiological pH. Nucleic Acids Res. *33*, 3025–3032.

14. Ohkubo, A., Yamada, K., Ito, Y., Yoshimura, K., Miyauchi, K., Kanamori, T., Masaki, Y., Seio, K., Yuasa, H., and Sekine, M. (2015). Synthesis and triplex-forming properties of oligonucleotides capable of recognizing corresponding DNA duplexes containing four base pairs. Nucleic Acids Res. *43*, 5675–5686.

15. Vuyisich, M., and Beal, P.A. (2000). Regulation of the RNA-dependent protein kinase by triple helix formation. Nucleic Acids Res. *28*, 2369–2374.

16. Fox, K.R., and Brown, T. (2011). Formation of stable DNA triplexes. Biochem. Soc. Trans. *39*, 629–634.

17. Zhou, Y., Kierzek, E., Loo, Z.P., Antonio, M., Yau, Y.H., Chuah, Y.W., Geifman-Shochat, S., Kierzek, R., and Chen, G. (2013). Recognition of RNA duplexes by chemically modified triplex-forming oligonucleotides. Nucleic Acids Res. *41*, 6664–6673.

18. Han, H., and Dervan, P.B. (1993). Sequence-specific recognition of double helical RNA and RNA.DNA by triple helix formation. Proc. Natl. Acad. Sci. USA *90*, 3806–3810.

19. Roberts, R.W., and Crothers, D.M. (1992). Stability and properties of double and triple helices: dramatic effects of RNA or DNA backbone composition. Science *258*, 1463–1466.

20. Escude, C., Francois, J.C., Sun, J.S., Ott, G., Sprinzl, M., Garestier, T., and Helene, C. (1993). Stability of triple helices containing RNA and DNA strands: experimental and molecular modeling studies. Nucleic Acids Res. *21*, 5547–5553.

21. Zhan, X., Deng, L., and Chen, G. (2022). Mechanisms and applications of peptide

nucleic acids selectively binding to double-stranded RNA. Biopolymers *113*, e23476.

22. Devi, G., Yuan, Z., Lu, Y., Zhao, Y., and Chen, G. (2014). Incorporation of thio-pseudoisocytosine into triplex-forming peptide nucleic acids for enhanced recognition of RNA duplexes. Nucleic Acids Res. *42*, 4008–4018.

23. Ong, A.A.L., Toh, D.F.K., Patil, K.M., Meng, Z., Yuan, Z., Krishna, M.S., Devi, G., Haruehanroengra, P., Lu, Y., Xia, K., et al. (2019). General Recognition of U-G, U-A, and C-G Pairs by Double-Stranded RNA-Binding PNAs Incorporated with an Artificial Nucleobase. Biochemistry *58*, 1319–1331.

24. Nielsen, P.E., Egholm, M., Berg, R.H., and Buchardt, O. (1991). Sequence-selective recognition of DNA by strand displacement with a thymine-substituted polyamide. Science *254*, 1497–1500.

25. Egholm, M., Buchardt, O., Christensen, L., Behrens, C., Freier, S.M., Driver, D.A., Berg, R.H., Kim, S.K., Norden, B., and Nielsen, P.E. (1993). PNA hybridizes to complementary oligonucleotides obeying the Watson–Crick hydrogen-bonding rules. Nature *365*, 566–568.

26. Swenson, C.S., Lackey, H.H., Reece, E.J., Harris, J.M., Heemstra, J.M., and Peterson, E.M. (2021). Evaluating the effect of ionic strength on PNA:DNA duplex formation kinetics. RSC Chem. Biol. *2*, 1249–1256.

27. Dragulescu-Andrasi, A., Rapireddy, S., Frezza, B.M., Gayathri, C., Gil, R.R., and Ly, D.H. (2006). A simple gamma-backbone modification preorganizes peptide nucleic acid into a helical structure. J. Am. Chem. Soc. *128*, 10258–10267.

28. Fabani, M.M., Abreu-Goodger, C., Williams, D., Lyons, P.A., Torres, A.G., Smith, K.G.C., Enright, A.J., Gait, M.J., and Vigorito, E. (2010). Efficient inhibition of miR-155 function in vivo by peptide nucleic acids. Nucleic Acids Res. *38*, 4466–4475.

29. Cheng, C.J., Bahal, R., Babar, I.A., Pincus, Z., Barrera, F., Liu, C., Svoronos, A., Braddock, D.T., Glazer, P.M., Engelman, D.M., et al. (2015). MicroRNA silencing for cancer therapy targeted to the tumour microenvironment. Nature *518*, 107–110.

30. Quijano, E., Bahal, R., Ricciardi, A., Saltzman, W.M., and Glazer, P.M. (2017). Therapeutic Peptide Nucleic Acids: Principles, Limitations, and Opportunities. Yale J. Biol. Med. *90*, 583–598.

31. Gupta, A., Quijano, E., Liu, Y., Bahal, R., Scanlon, S.E., Song, E., Hsieh, W.C., Braddock, D.E., Ly, D.H., Saltzman, W.M., and Glazer, P.M. (2017). Anti-tumor Activity of miniPEG-γ-Modified PNAs to Inhibit MicroRNA-210 for Cancer Therapy. Mol. Ther. Nucleic Acids *9*, 111–119.

32. Ricciardi, A.S., Bahal, R., Farrelly, J.S., Quijano, E., Bianchi, A.H., Luks, V.L., Putman, R., López-Giráldez, F., Coşkun, S., Song, E., et al. (2018). In utero nanoparticle delivery for site-specific genome editing. Nat. Commun. *9*, 2481.

33. Wang, Y., Malik, S., Suh, H.W., Xiao, Y., Deng, Y., Fan, R., Huttner, A., Bindra, R.S., Singh, V., Saltzman, W.M., and Bahal, R. (2023). Anti-seed PNAs targeting multiple oncomiRs for brain tumor therapy. Sci. Adv. *9*, eabq7459.

34. Brazil, R. (2023). Peptide Nucleic Acids Promise New Therapeutics and Gene Editing Tools. ACS Cent. Sci. *9*, 3–6.

35. Lu, R., and Chen, G. (2024). Pre-twisting for improved genome modification and miRNA targeting. Trends Biochem. Sci. *49*, 283–285.

36. Toh, D.F.K., Devi, G., Patil, K.M., Qu, Q., Maraswami, M., Xiao, Y., Loh, T.P., Zhao, Y., and Chen, G. (2016). Incorporating a guanidine-modified cytosine base into triplex-forming PNAs for the recognition of a C-G pyrimidine-purine inversion site of an RNA duplex. Nucleic Acids Res. *44*, 9071–9082.

37. Patil, K.M., Toh, D.F.K., Yuan, Z., Meng, Z., Shu, Z., Zhang, H., Ong, A.A.L., Krishna, M.S., Lu, L., Lu, Y., and Chen, G. (2018). Incorporating uracil and 5-halouracils into short peptide nucleic acids for enhanced recognition of A-U pairs in dsRNAs. Nucleic Acids Res. *46*, 7506–7521.

38. Kesy, J., Patil, K.M., Kumar, S.R., Shu, Z., Yong, H.Y., Zimmermann, L., Ong, A.A.L., Toh, D.F.K., Krishna, M.S., Yang, L., et al. (2019). A Short Chemically Modified dsRNA-Binding PNA (dbPNA) Inhibits Influenza Viral Replication by Targeting Viral RNA Panhandle Structure. Bioconjugate Chem. *30*, 931–943.

39. Ong, A.A.L., Toh, D.F.K., Krishna, M.S., Patil, K.M., Okamura, K., and Chen, G. (2019). Incorporating 2-Thiouracil into Short Double-Stranded RNA-Binding Peptide Nucleic Acids for Enhanced Recognition of A-U Pairs and for Targeting a MicroRNA Hairpin Precursor. Biochemistry *58*, 3444–3453.

40. Li, M., Zengeya, T., and Rozners, E. (2010). Short Peptide Nucleic Acids Bind Strongly to Homopurine Tract of Double Helical RNA at pH 5.5. J. Am. Chem. Soc. *132*, 17052.

41. Gupta, P., Zengeya, T., and Rozners, E. (2011). Triple helical recognition of pyrimidine inversions in polypurine tracts of RNA by nucleobase-modified PNA. Chem. Commun. *47*, 11125–11127.

42. Zengeya, T., Gupta, P., and Rozners, E. (2012). Triple-Helical Recognition of RNA Using 2-Aminopyridine-Modified PNA at Physiologically Relevant Conditions. Angew Chem. Int. Ed. Engl. *51*, 12593–12596.

43. Zengeya, T., Gupta, P., and Rozners, E. (2014). Sequence selective recognition of double-stranded RNA using triple helix-forming peptide nucleic acids. Methods Mol. Biol. *1050*, 83–94.

44. Brodyagin, N., Katkevics, M., Kotikam, V., Ryan, C.A., and Rozners, E. (2021). Chemical approaches to discover the full potential of peptide nucleic acids in biomedical applications. Beilstein J. Org. Chem. *17*, 1641–1688.

45. Sato, T., Sato, Y., and Nishizawa, S. (2016). Triplex-Forming Peptide Nucleic Acid Probe Having Thiazole Orange as a Base Surrogate for Fluorescence Sensing of Double-stranded RNA. J. Am. Chem. Soc. *138*, 9397–9400.

46. Lopez-Tena, M., Chen, S.K., and Winssinger, N. (2023). Supernatural: Artificial Nucleobases and Backbones to Program Hybridization-Based Assemblies and Circuits. Bioconjugate Chem. *34*, 111–123.

47. Katkevics, M., MacKay, J.A., and Rozners, E. (2024). Triplex-forming peptide nucleic acids as emerging ligands to modulate structure and function of complex RNAs. Chem. Commun. *60*, 1999–2008.

48. Puah, R.Y., Jia, H., Maraswami, M., Toh, D.F.K., Ero, R., Yang, L., Patil, K.M., Ong, A.A.L., Krishna, M.S., Sun, R., et al. (2018). Selective Binding to mRNA Duplex Regions by Chemically Modified Peptide Nucleic Acids Stimulates Ribosomal Frameshifting. Biochemistry *57*, 149–159.

49. Endoh, T., Hnedzko, D., Rozners, E., and Sugimoto, N. (2016). Nucleobase-Modified PNA Suppresses Translation by Forming a Triple Helix with a Hairpin Structure in mRNA In Vitro and in Cells. Angew Chem. Int. Ed. Engl. *55*, 899–903.

50. Endoh, T., Brodyagin, N., Hnedzko, D., Sugimoto, N., and Rozners, E. (2021). Triple-Helical Binding of Peptide Nucleic Acid Inhibits Maturation of Endogenous MicroRNA-197. ACS Chem. Biol. *16*, 1147–1151.

51. Tay, D.J.T., Song, Y., Peng, B., Toh, T.B., Hooi, L., Toh, D.F.K., Hong, H., Tang, S.J., Han, J., Gan, W.L., et al. (2021). Targeting RNA editing of antizyme inhibitor 1: A potential oligonucleotide-based antisense therapy for cancer. Mol. Ther. *29*, 3258–3273.

52. Krishna, M.S., Wang, Z., Zheng, L., Bowry, J., Ong, A.A.L., Mu, Y., Prabakaran, M., and Chen, G. (2019). Incorporating G-C Pair-Recognizing Guanidinium into PNAs for Sequence and Structure Specific Recognition of dsRNAs over dsDNAs and ssRNAs. Biochemistry *58*, 3777–3788.

53. Abraham, M.J., Murtola, T., Schulz, R., Páll, S., Smith, J.C., Hess, B., and Lindahl, E. (2015). GROMACS: High performance molecular simulations through multi-level parallelism from laptops to supercomputers. SoftwareX *1–2*, 19–25.

54. Jasinski, M., Feig, M., and Trylska, J. (2018). Improved Force Fields for Peptide Nucleic Acids with Optimized Backbone Torsion Parameters. J. Chem. Theor. Comput. *14*, 3603–3620.

55. Bhatt, P.R., Scaiola, A., Loughran, G., Leibundgut, M., Kratzel, A., Meurs, R., Dreos, R., O'Connor, K.M., McMillan, A., Bode, J.W., et al. (2021). Structural basis of ribosomal frameshifting during translation of the SARS-CoV-2 RNA genome. Science *372*, 1306–1313.

56. Sun, Y., Abriola, L., Niederer, R.O., Pedersen, S.F., Alfajaro, M.M., Silva Monteiro, V., Wilen, C.B., Ho, Y.C., Gilbert, W.V., Surovtseva, Y.V., et al. (2021). Restriction of SARS-CoV-2 replication by targeting programmed -1 ribosomal frameshifting. Proc. Natl. Acad. Sci. USA *118*, e2023051118.

57. Kelly, J.A., Woodside, M.T., and Dinman, J.D. (2021). Programmed -1 Ribosomal Frameshifting in coronaviruses: A therapeutic target. Virology *554*, 75–82.

58. Jacks, T., and Varmus, H.E. (1985). Expression of the Rous sarcoma virus pol gene by ribosomal frameshifting. Science *230*, 1237–1242.

59. Larsen, B., Gesteland, R.F., and Atkins, J.F. (1997). Structural probing and mutagenic

analysis of the stem-loop required for Escherichia coli dnaX ribosomal frameshifting: programmed efficiency of 50. J. Mol. Biol. *271*, 47–60.

60. Brierley, I., Digard, P., and Inglis, S.C. (1989). Characterization of an efficient coronavirus ribosomal frameshifting signal: requirement for an RNA pseudoknot. Cell *57*, 537–547.

61. Grentzmann, G., Ingram, J.A., Kelly, P.J., Gesteland, R.F., and Atkins, J.F. (1998). A dual-luciferase reporter system for studying recoding signals. RNA *4*, 479–486.

62. Zhong, Z., Yang, L., Zhang, H., Shi, J., Vandana, J.J., Lam, D.T.U.H., Olsthoorn, R.C.L., Lu, L., and Chen, G. (2016). Mechanical unfolding kinetics of the SRV-1 gag-pro mRNA pseudoknot: possible implications for -1 ribosomal frameshifting stimulation. Sci. Rep. *6*, 39549.

63. Qu, X., Wen, J.D., Lancaster, L., Noller, H.F., Bustamante, C., and Tinoco, I., Jr. (2011). The ribosome uses two active mechanisms to unwind messenger RNA during translation. Nature *475*, 118–121.

64. Amiri, H., and Noller, H.F. (2019). A tandem active site model for the ribosomal helicase. FEBS Lett. *593*, 1009–1019.

65. Rehfeld, F., Eitson, J.L., Ohlson, M.B., Chang, T.C., Schoggins, J.W., and Mendell, J.T. (2023). CRISPR screening reveals a dependency on ribosome recycling for efficient SARS-CoV-2 programmed ribosomal frameshifting and viral replication. Cell Rep. *42*, 112076.

66. Sundaram, G.M., Common, J.E.A., Gopal, F.E., Srikanta, S., Lakshman, K., Lunny, D.P., Lim, T.C., Tanavde, V., Lane, E.B., and Sampath, P. (2013). 'See-saw' expression of microRNA-198 and FSTL1 from a single transcript in wound healing. Nature *495*, 103–106.

67. Grover, A., Houlden, H., Baker, M., Adamson, J., Lewis, J., Prihar, G., Pickering-Brown, S., Duff, K., and Hutton, M. (1999). 5' splice site mutations in tau associated with the inherited dementia FTDP-17 affect a stem-loop structure that regulates alternative splicing of exon 10. J. Biol. Chem. *274*, 15134–15143.

68. Varani, L., Hasegawa, M., Spillantini, M.G., Smith, M.J., Murrell, J.R., Ghetti, B., Klug, A., Goedert, M., and Varani, G. (1999). Structure of tau exon 10 splicing regulatory element RNA and destabilization by mutations of frontotemporal dementia and parkinsonism linked to chromosome 17. Proc. Natl. Acad. Sci. USA *96*, 8229–8234.

69. Donahue, C.P., Muratore, C., Wu, J.Y., Kosik, K.S., and Wolfe, M.S. (2006). Stabilization of the tau exon 10 stem loop alters pre-mRNA splicing. J. Biol. Chem. *281*, 23302–23306.

70. Tan, J., Yang, L., Ong, A.A.L., Shi, J., Zhong, Z., Lye, M.L., Liu, S., Lisowiec-Wachnicka, J., Kierzek, R., Roca, X., and Chen, G. (2019). A Disease-Causing Intronic Point Mutation C19G Alters Tau Exon 10 Splicing via RNA Secondary Structure Rearrangement. Biochemistry *58*, 1565–1578.

71. Hutton, M., Lendon, C.L., Rizzu, P., Baker, M., Froelich, S., Houlden, H., Pickering-Brown, S., Chakraverty, S., Isaacs, A., Grover, A., et al. (1998). Association of missense and 5'-splice-site mutations in tau with the inherited dementia FTDP-17. Nature *393*, 702–705.

72. Schoch, K.M., DeVos, S.L., Miller, R.L., Chun, S.J., Norrbom, M., Wozniak, D.F., Dawson, H.N., Bennett, C.F., Rigo, F., and Miller, T.M. (2016). Increased 4R-Tau Induces Pathological Changes in a Human-Tau Mouse Model. Neuron *90*, 941–947.

73. McCarthy, A., Lonergan, R., Olszewska, D.A., O'Dowd, S., Cummins, G., Magennis, B., Fallon, E.M., Pender, N., Huey, E.D., Cosentino, S., et al. (2015). Closing the tau loop: the missing tau mutation. Brain *138*, 3100–3109.

74. Ong, A.A.L., Tan, J., Bhadra, M., Dezanet, C., Patil, K.M., Chong, M.S., Kierzek, R., Decout, J.L., Roca, X., and Chen, G. (2019). RNA Secondary Structure-Based Design of Antisense Peptide Nucleic Acids for Modulating Disease-Associated Aberrant Tau Pre-mRNA Alternative Splicing. Molecules *24*, 3020.

75. Eldrup, A.B., Dahl, O., and Nielsen, P.E. (1997). A novel peptide nucleic acid monomer for recognition of thymine in triple-helix structures. J. Am. Chem. Soc. *119*, 11116–11117.

76. Liu, Z., Wang, J., Cheng, H., Ke, X., Sun, L., Zhang, Q.C., and Wang, H.W. (2018). Cryo-EM Structure of Human Dicer and Its Complexes with a Pre-miRNA Substrate. Cell *173*, 1549–1550.